

Filterless Nondispersive Infrared Sensing using Narrowband Infrared Emitting Metamaterials

Alyssa Livingood,[■] J. Ryan Nolen,[■] Thomas G. Folland, Lauren Potechin, Guanyu Lu, Scott Criswell, Jon-Paul Maria, Christopher T. Shelton, Edward Sachet, and Joshua D. Caldwell*



Cite This: *ACS Photonics* 2021, 8, 472–480



Read Online

ACCESS |



Metrics & More



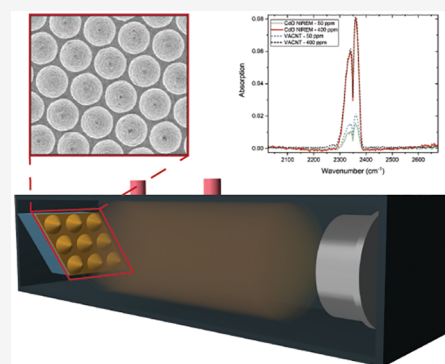
Article Recommendations



Supporting Information

ABSTRACT: For many industrial and manufacturing applications, detecting and identifying low concentrations of harmful gases and byproducts are performed using nondispersive infrared (NDIR) sensors. These simple devices utilize a broadband IR emitter, thermopile detector, and a spectrally narrow bandpass filter tuned to a vibrational resonance of the analyte of interest. However, such filters are expensive to fabricate and limit the NDIR to operation at only a single frequency, unless filter wheels are employed, which expand the size and complexity of the device considerably. Here, we create a nanophotonic infrared emitting metamaterial (NIREM) fabricated from thin films of doped CdO grown on patterned sapphire substrates (PSS) that exhibit narrowband thermal emission. By coupling a sufficiently narrow line width emitter with a simple broadband detector such as a thermopile, the functionality of the NDIR sensor can be replicated without the need for the narrow bandpass filter. Unlike many metamaterial-based emitters, our device emits both *p*- and *s*-polarized light with near-unity emissivity at angles ranging from 0° to 40° off the surface normal without complicated and expensive lithography steps. As a proof of concept, we implement this NIREM for CO₂ gas detection within an FTIR spectrometer, demonstrating performance comparable with a conventional blackbody/filter combination. This demonstrates that the NIREM concept can provide a suitable plug-and-play replacement for NDIR devices as they can be implemented in a form-factor commensurate or significantly reduced in comparison to the current state of the art. In principle, by incorporating multiple NIREM dies tuned to emit at different frequencies, multiple vibrational modes could be sequentially detected, making the approach amenable to identification and quantification of complicated molecules within a single NDIR configuration.

KEYWORDS: thermal emission, epsilon-near-zero, mid-infrared, optical gas sensing, metamaterials



INTRODUCTION

Molecular sensing plays a critical role in a variety of applications such as chemical and industrial manufacturing, oil and gas exploration and extraction, defense and security, as well as environmental safety. Many schemes exist for the detection of chemical species, and for gases with characteristic absorption bands within the infrared, optical spectroscopy is commonly used and has advantages over other techniques.¹ Typically, this is achieved through exploitation of the Beer–Lambert law; a reduction in the transmission of IR light resonant with a molecular vibrational absorption over a defined cross-sectional area and path length is directly proportional to the concentration of that molecule. This inherently implies that for infrared detection there is a need for either a spectroscopic solution, such as Fourier transform infrared (FTIR) spectroscopy, or a single frequency excitation/detection scheme. In the case of the latter, a number of potential solutions arise: (1) implementation of a broadband light source and detector pair, with a narrow bandpass filter (see Figure 1a), (2) implementation of a narrow band detector with a broadband source,^{2,3} or (3) use a narrow band source

with a broadband detector (Figure 1b). The first solution is the basis for nondispersive infrared (NDIR) gas sensors that are widely implemented in industry because of their device simplicity.⁴ A platform supporting both a narrow band source and detector pair, such as the MEMS-based sensor designed by Lochbaum et al.,⁵ is another potential solution. However, these come with the inherent limitation of only operating at a single fixed frequency, and the inclusion of sufficiently narrow bandpass filters results in significant increases in cost. Multiple frequencies can be measured via NDIR through the incorporation of a filter wheel featuring multiple bandpass filters; however, this significantly increases the cost, size, and complexity of the device. In such dual narrow bandwidth approaches the signal-to-noise ratio is enhanced resulting in

Received: September 15, 2020

Published: January 13, 2021



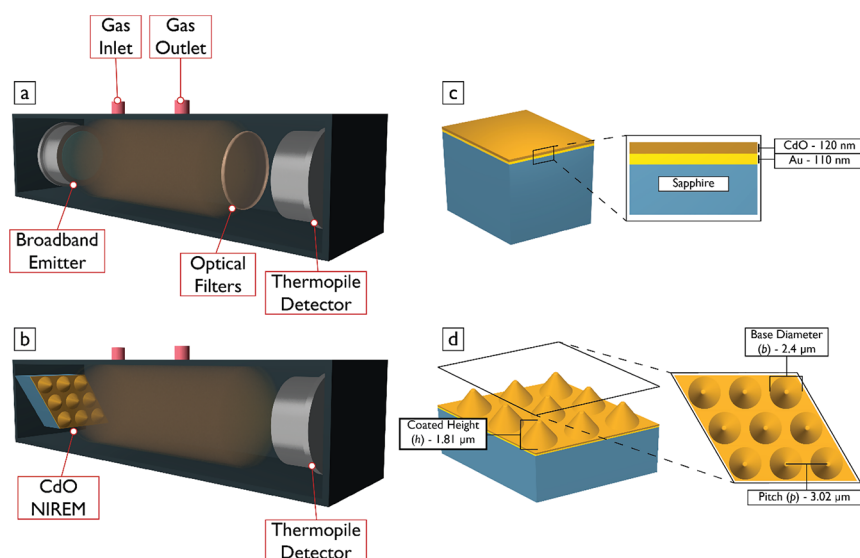


Figure 1. (a) Schematic of conventional NDIR sensor. (b) Proposed NIREM-enabled NDIR sensor design. (c) Perspective view and cross-section of 120 nm In:CdO film deposited onto 110 nm Au-coated flat sapphire substrate. The same layer thicknesses were deposited onto the PSS substrate sample depicted in panel d. Here, we provide a perspective and top-view of the PSS sample, with geometry labeled.

similar sensitivity and selectivity to conventional methods in a significantly smaller device. However, the single narrow bandwidth resonance supported by the emitter and detector precludes multifrequency operation and typically comes with significant increases in design complexity and expense. Thus, ideally, an NDIR approach would implement a simple, inexpensive, narrowband source or detector to eliminate these challenges, while still maintaining the standard form factor and sensitivity of commercial NDIR systems.

One obvious solution to eliminate the need for a narrow bandpass filter within NDIR designs is to integrate a similarly narrow bandwidth detector. Such systems have been demonstrated using a broad range of materials, for instance graphene resonator designs and plasmonic resonant structures.^{2,6} However, this requires extensive nanoscale lithographic fabrication, resulting in increases in cost and complexity, while in many cases also limiting the absorptivity of the device. A similar, but arguably more powerful approach is to integrate Bragg mirrors in order to resonantly enhance detection, but this requires the accurate growth of thick mirror layers.² Alternatively, one could utilize a narrow band source, for example by incorporating an IR laser; however, within the molecular fingerprint window ($500\text{--}3500\text{ cm}^{-1}$), this requires quantum cascade lasers (QCLs) or gas lasers,⁷ both of which have large electrical power requirements. While it is possible to make extremely sensitive gas sensors using these devices, such solutions are less palatable for most industrial settings where low cost and compact solutions are absolutely required for commercial viability. Midinfrared LEDs have become increasingly more appealing for such applications; however, these devices still have low output power and relatively broadband emission, which results in a high probability of cross-talk with other absorbing gases. Recently, photonic crystals,^{8–10} polaritonic,^{11–14} and metamaterial^{15,16} designs have been employed to control thermal emissivity and realize narrowband IR sources.¹⁷ These nanophotonic infrared emitting metamaterials (NIREMs) have been designed to exhibit line widths approaching that of the molecular vibrations themselves,^{13,18} illustrating the potential for targeted and

sensitive measurements. Recently, such metamaterials implementing the so-called perfect absorber geometry^{19,20} were demonstrated for an advanced NDIR approach, illustrating similar sensitivity to CO_2 as commercial devices, without the requirement of the aforementioned bandpass filter.²¹ Yet, in that work, electron beam lithography was required to fabricate the metallic nanostructures necessary to stimulate the localized surface plasmon polariton (SPP) resonances within the mid-IR, the spectral range for which this device was designed.

Here we demonstrate that our NIREM concept overcomes each of the previously mentioned challenges, enabling a potential plug-and-play platform for direct replacements of current NDIR devices. This is realized through the narrowband, near-unity absorption of both *p*- and *s*-polarized light (>0.95 from 0 to 40° off the surface normal) facilitated via epsilon-near-zero (ENZ) modes^{22,23} within thin films ($<150\text{ nm}$) of *n*-type, In-doped CdO (In:CdO) grown on patterned sapphire substrates (PSS). A side and top-view schematic of the coated PSS structure is shown in Figure 1d. These modes can be spectrally tuned from approximately $2\text{--}10\ \mu\text{m}$ free-space wavelengths ($5000\text{--}1000\text{ cm}^{-1}$) in CdO via doping,^{24–26} allowing these devices to target essentially the full fingerprint region. Similarly, narrowband single and multifrequency thermal emission has been demonstrated in ultrathin, Berreman-mode-supporting CdO films and multilayer stacks, respectively.²⁷ However, in flat films these Berreman excitations couple only to *p*-polarized light and exhibit highly off-normal emission angles, with the emissivity peaking near the Brewster condition ($\sim 65^\circ$). By growing the ENZ CdO film upon a PSS, the thermal emission is no longer restricted to angles around the Brewster angle, instead resulting in ENZ-polariton modes that emit over a hemisphere, with the strongest emission occurring around the surface normal. If illuminated at normal incidence, scattering from the conical structures of the PSS results in the excitation of the ENZ mode in the CdO film. Reciprocally, through Kirchhoff's law, the cylindrical symmetry of the PSS cones allows for the out-coupling of both *s*- and *p*-polarized emission from the thermal excitation of the ENZ mode. While the periodicity of the PSS

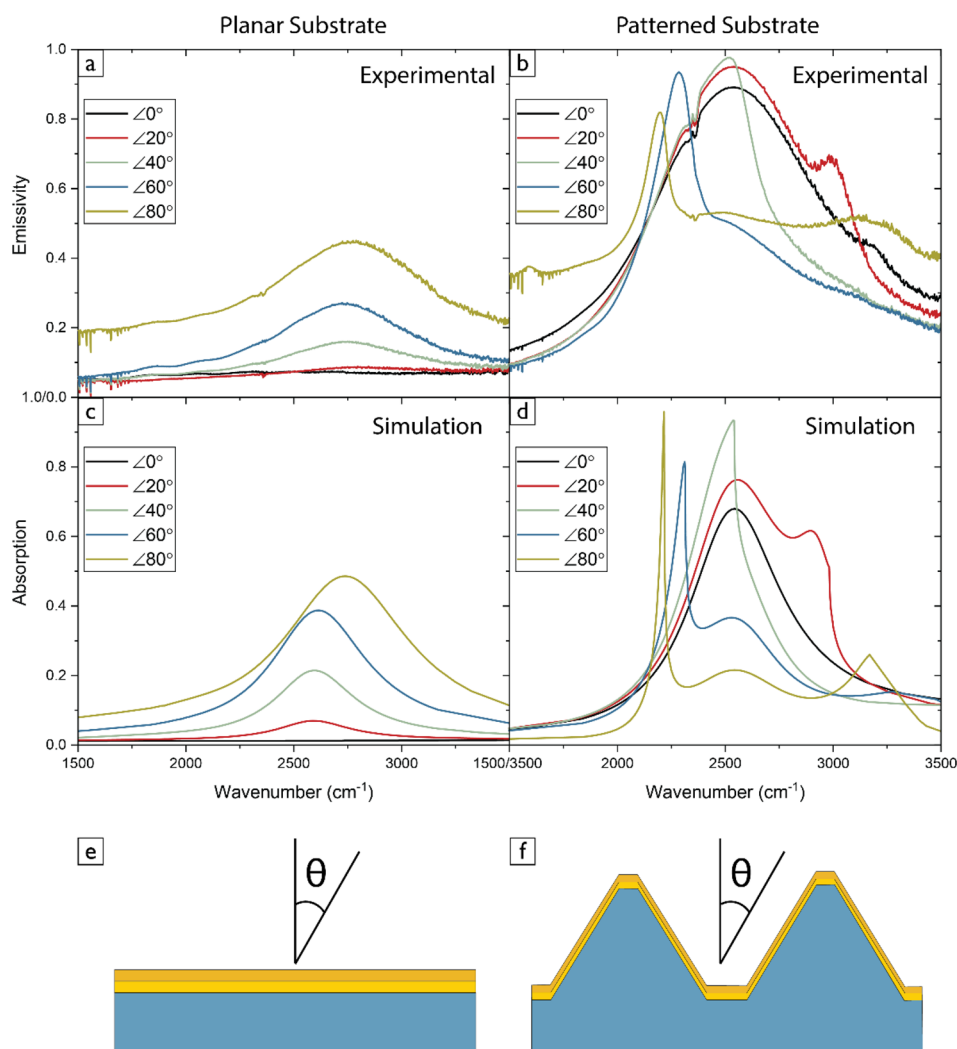


Figure 2. (a) Angle-dependent thermal emission measurements of the flat CdO film sample shown in panel e. (b) Angle-dependent thermal emission measurements of the CdO on PSS sample shown in panel f. Panels c and d display the simulated angle-dependent absorption spectra for the flat CdO and CdO on PSS samples, respectively. The feature seen at 2349 cm^{-1} in panels a and b is due to absorption from ambient CO_2 .

structuring does induce some angular dispersion in the spectra, this is primarily observed at the steepest angles, and thus induces minimal influence upon the NDIR response normal to the surface. Finally, we provide a proof-of-principle experiment illustrating the detection of CO_2 using the NIREM device, demonstrating similar sensitivity to that of a broadband emitter used in a standard NDIR detector. These experiments illustrate the potential for the NIREM devices as a direct IR source replacement for the broadband emitter in conventional NDIR devices. This enables the elimination of the bandpass filter as well as offering the opportunity to realize next generation devices offering multifrequency detection (through depositing multiple films on the same sample, or multiple die combined into a single NDIR architecture) within the same gas cell.

RESULTS AND DISCUSSION

Our NIREM device is based on the strong absorption of the Berreman and ENZ-polariton modes within thin films of polaritonic media. The Berreman mode, along with the ENZ polariton mode that is its subdiffractional counterpart, are the result of strong coupling between surface polaritons supported on the opposing interfaces of a thin film.²² Thin films of In: CdO on the order of 120 nm thick (Figure 1c) support both

Berreman and ENZ modes, with the former being accessible from free-space and providing near-unity absorption of p -polarized light at angles near the Brewster angle.²⁷ The ENZ dispersion exists outside of the free-space light cone, requiring auxiliary momentum in order to be accessed. The calculated Berreman/ENZ modal dispersion is provided in Figure S4. In our work, we observe strong emission from such a 120 nm thick $N_d = 5.8 \times 10^{19}\text{ cm}^{-3}$ In: CdO film that is derived from this dispersion relation, as discussed below. The experimentally measured and numerically calculated emission from our thin film CdO are shown in Figure 2a and c, respectively. As the emission spectra provided in Figure 2a is unpolarized, an emissivity at close to 0.5 implies near-unity absorption of p -polarized light through Kirchhoff's law, at an angle of approximately 70° (see polarized thermal emission spectra in Figure S1). However, such steep emission angles are nonideal for NDIR applications, as the majority of the light will be emitted toward the gas cell wall, rather than being directed toward the detector. Adjustments could be made to account for this off-normal emission from the flat film, such as the incorporation of a wedge to direct the emission toward the detector, yet this would inherently reduce the collected power or require high numerical aperture collection optics to

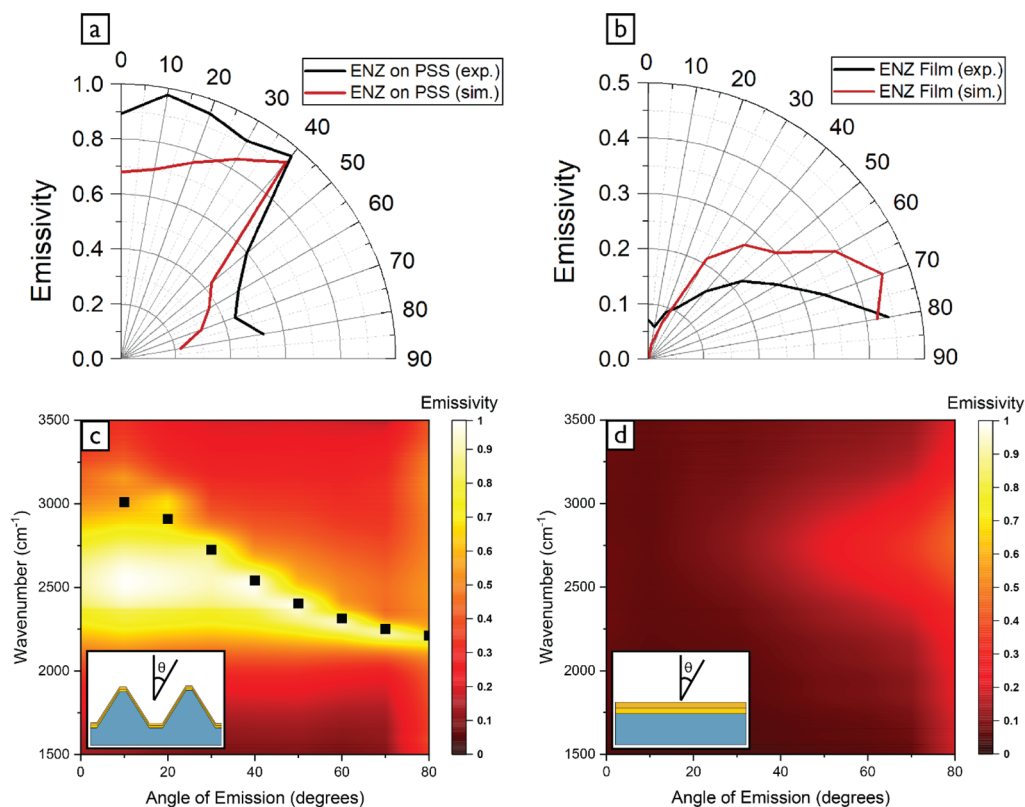


Figure 3. Polar peak emissivity plots for the (a) CdO on PSS and (b) CdO flat film samples. The black line represents the measured angle-dependent, unpolarized emissivity and red line is the simulated angle-dependent, unpolarized absorption. Contour plots showing the measured emissivity of the CdO PSS NIREM and CdO Berreman film are displayed in panels (c) and (d). The simulated frequencies of the diffractive mode are included as the black squares in (c).

overcome. Furthermore, the possible collected power is still limited to below 50% as the Berreman mode only couples to *p*-polarized light. Thus, for the NDIR application an alternative device design is required if such challenges are to be overcome.

To enable strong thermal emission of both *p*- and *s*-polarized light, designs exploiting different types of physics have been employed. One method broadly implemented in the perfect absorber geometry is to utilize a cross-shaped polaritonic resonator, whereby each arm of the cross can couple to the orthogonal polarization states. When combined with a dielectric spacer and metallic back plane, perfect absorption can be realized.^{19,20} Indeed, this was the geometry utilized by Lochbaum et al.^{5,21} for demonstrating a narrowband emitter and detector for an advanced NDIR scheme. However, as noted above, for such structures to provide polaritonic resonances in the mid-IR, advanced lithographic tools and typically costly plasmonic metals are required. Alternatively, one could envision realizing nanostructures through growth of a polaritonic medium on a periodically textured surface. However, this approach has not been employed for such a device due to the challenges associated with epitaxy on such a nonplanar surface. This would inherently result in an increase in defect density and a propensity to form polycrystalline, rather than single crystal epitaxial films, which in turn result in increases in optical loss. Here, CdO offers substantial benefits as it has been previously demonstrated that for highly doped CdO ($>1 \times 10^{19} \text{ cm}^{-3}$) increases in doping density result in an increased effective mass, while also maintaining the large electron mobilities ($\mu > 300 \text{ cm}^2/\text{V}\cdot\text{s}$) and thus reductions in optical losses, even at significantly elevated carrier densities in

excess of $3 \times 10^{20} \text{ cm}^{-3}$.²⁸ Furthermore, this material offers a propensity for high-quality growth via high power, impulse magnetron sputtering (HiPIMS) on a variety of substrates, including nonplanar structures and metal films while maintaining the low loss tangents that highlight the promise of this material.^{24,25}

Because of the requirement of NDIR sensors to be inexpensive, any structured surface must be one that can be realized via scalable, low-cost methods on large-area substrates. Patterned sapphire substrates offer such a template as the structured surface is the result of wet chemical treatment in H_2SO_4 at elevated temperatures ($\sim 240 \text{ }^\circ\text{C}$) or plasma-based dry etching techniques,²⁹ and are commercially available at up to 8-in. wafers at low cost. For the purpose of testing the spectral and spatial emissivity of an ENZ CdO film when grown on such a PSS substrate, a 120 nm thick n-type In:CdO film was grown via HiPIMS on a PSS substrate that had first been coated with a 110 nm thick sputtered gold layer. A schematic of the PSS cone cross-section along with scanning electron microscope (SEM) images of the coated structure are provided in Figure S6. Note that the layer thicknesses and material stacking order are identical for the CdO flat film and PSS samples. The PSS substrates used consisted of a periodic array (pitch $p = 3.02 \text{ } \mu\text{m}$) of circular-base ($b = 2.4 \text{ } \mu\text{m}$) conical structures with an uncoated height of $1.58 \text{ } \mu\text{m}$. A top-view schematic of the gold/CdO-coated structure is depicted in Figure 1d. Note, in contrast to the flat Berreman-supporting film (Figure 2a and c), when the same film is grown on the PSS, several significant modifications are realized (Figure 2b and d, respectively). First, as noted above, the structuring of

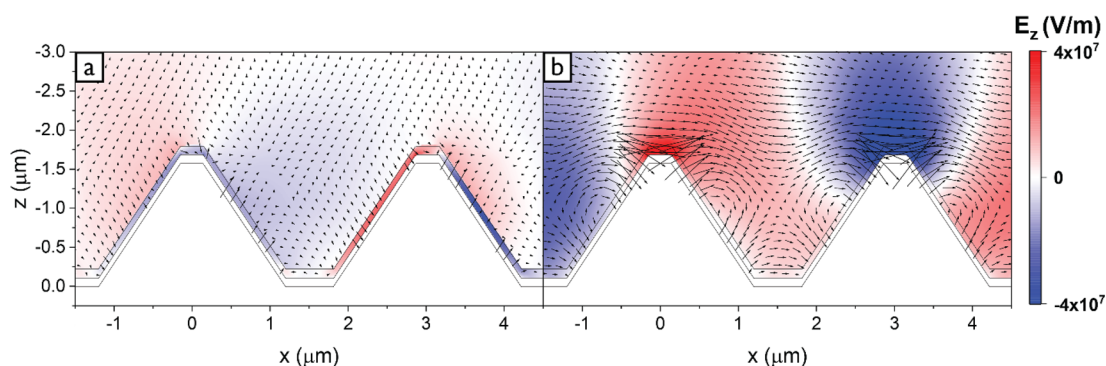


Figure 4. (a) Z-oriented electric field (E_z) and Poynting vector (\vec{S}) of ENZ mode (2550 cm^{-1}). (b) Z-oriented E_z and \vec{S} of diffractive mode (3000 cm^{-1}). Both field profiles were simulated at a 20° angle of incident.

the film results in near-unity emissivity (absorptivity) from near-normal incidence up to approximately 40° off-normal (Figure 3a). The symmetric, conical shape of the structures also enables out-coupling of both p - and s -polarized light on resonance with high efficiencies. Further, the emission along the sidewalls of the cones is partially directed back toward the substrate and adjacent cones, resulting in reabsorption into the ENZ mode and emission enhancement at near-normal emission angles. As the angle is increased away from the surface normal, a significant narrowing of the resonant mode is observed due to interference between the dispersive diffractive and nondispersive ENZ resonant modes as can be seen in Figure 2b, as well as in the contour plot presented in Figure 3c. The slight difference in emission frequencies between the flat film and PSS sample is a result of the Berreman/ENZ origin of these modes. Because of the anticrossing at the intersection²² of the plasma frequency and light line in air (see Figure S4), the Berreman mode is excited slightly above and ENZ-polariton just below the plasma frequency in polaritonic films, with the magnitude of this shift being dependent upon the film thickness. The resonant frequencies are therefore slightly offset from the plasma frequency, but in opposite directions spectrally. Also, note that the measured emission and simulated absorption (Figure 2a and 2c, respectively) of the planar film exhibits a slight blue shift at high emission angles. This is due to the corresponding blue shift of the Berreman mode as the dispersion approaches the light line from the left ($k/k_0 < 1$). This is in contrast to the nondispersive thermal emission from the PSS sample, which is the result of the excitation of the ENZ-polariton mode described above. These angle-dependent thermal emission measurements were performed using a motorized, angle-resolved thermal emission rig that was built in-house and coupled to the existing Bruker Vertex 70v FTIR spectrometer. The measured baseline emissivity is slightly elevated at high emission angles (80°), which is due to the collection of the emission from the hot plate behind the sample. At these large emission angles the spot size (5 mm) was slightly larger than the projection of the sample. A detailed description of the FTIR thermal emission measurements are provided in the Methods section, and a schematic of the thermal emission setup is provided in the Supporting Information.

The origin of the spectral narrowing is indicative of interference between the ENZ-polariton and the diffractive mode resulting from the periodic patterning^{30–32} of the PSS template. Indeed, such Fano-like interactions have been reported in a broad range of periodic arrays of polaritonic

resonators.^{33–36} To validate this claim, three-dimensional, finite-element-method electromagnetic simulations of the ENZ CdO layer on a PSS substrate were performed using CST Studio Suite. Here, a dielectric function model previously reported by our group²⁶ and the sample geometry presented in Figure 1d were implemented to determine the angle-dependent absorption spectra displayed in Figure 2d. Calculations of the angle-dependent absorption of the structure (Figure 2d) agree well with our experiments (Figure 2c). However, there are very slight differences between the measured emission and simulated absorption peak positions for both the planar film (Figure 2a and 2c) and PSS film (Figure 2b and 2d), which is due to the dielectric function employed for simulations not exactly matching that of this specific CdO film. From Figure 2b and 2d, it can be seen that the dispersive, diffractive mode effectively tunes through the ENZ polariton resonance, which maintains a nominally constant frequency, granting no indication of strong modal coupling. Note again that due to Kirchhoff's law these absorption spectra can be compared directly to the measured angle-dependent emissivity spectra. The simulated spectral positions of the diffractive mode are included as black squares overlaying the measured emissivity contour plot (Figure 3c) showing excellent agreement between measured and simulated values.

The origin of these resonant features as diffractive in nature is confirmed through comparison of the spectral dispersion at different grating pitches, with the diffractive mode shown to red shift as the pitch is increased (Figure S2). Additionally, cross-sectional field profiles of the z-oriented electric field (E_z), as well as the Poynting vector (\vec{S}) at the ENZ condition (2550 cm^{-1}) and, at the peak of the diffractive order, for angles of 20° (3000 cm^{-1}) are provided in Figure 4a and 4b, respectively, showing distinctly different resonant behavior. At the ENZ resonance (Figure 4a), a strong confinement of the electromagnetic fields is observed within the ENZ layer, with a clear dipolar character in the phase across the resonant structure. Further, the magnitude of \vec{S} is relatively small ($|S_{\text{max,ENZ}}| = 3.3 \times 10^{12}\text{ W/m}^2$) both inside and outside of the CdO layer, with an orientation matching that of the incident wave. However, at the diffractive resonance, the mode is identified as having a strong in-plane momentum, as indicated by the alignment and magnitude of \vec{S} ($|S_{\text{max,Diff}}| = 7.0 \times 10^{13}\text{ W/m}^2$) above the sample, and fields coupled between adjacent resonators consistent with a diffractive mode. However, while the presence of the diffractive modes induces some angular dispersion in the spectral emissivity, this is predominantly at steep angles in the spectral region of interest ($\omega \approx 2550\text{ cm}^{-1}$),

and thus, at angles within $\pm 40^\circ$ off normal, the emission spectra is still peaked at the ENZ condition with near-unity emissivity (Figure 3a and 3c). This diffractive order can be tuned spectrally by depositing an identical CdO film on a PSS featuring a different pitch. Thus, it is possible to design a CdO on PSS structure in which the grating resonance is non-interacting with the ENZ emission at larger off-normal angles or one featuring a strong overlap with the ENZ resonance at normal incidence as is shown in Figure S3.

On the basis of the near-unity, narrow bandwidth thermal emission resulting from the CdO PSS structure, and the redirection of both *p*- and *s*-polarized light within a radiation pattern directed at angles within 40° of the surface normal, it is clear that there is a high potential for this CdO-based NIREM device for advanced NDIR approaches. To validate this supposition, we implemented the external thermal emission input of our Bruker Vertex 70v FTIR spectrometer, integrating the thermal emission (250 °C) from the CdO-PSS device at the surface normal as the source. This was passed through the interferometer and a short-path gas cell from Pike Technologies and detected using an MCT detector. The sample compartment, which housed the gas cell, as well as the rest of the FTIR were kept under N_2 purge. Once the gas cell was adequately purged, CO_2 gas was passed through the cell using calibrated gas cylinders with 400 or 50 ppm of CO_2 in N_2 . To enable direct comparison with a more traditional blackbody-based NDIR approach, these results were compared with similar measurements performed using a vertically aligned carbon nanotube (VACNT) array blackbody (NanoTechLabs, Inc.) reference as the source. For more details about the gas cell measurements, see the Methods section.

The mid-infrared spectrum of CO_2 consists of two molecular vibrational modes corresponding to the antisymmetric stretching modes at 2349 and 3756 cm^{-1} .³⁷ As the collected spectra from the NIREM device is peaked at 2550 cm^{-1} , with a radiation pattern suitable for directing the light toward the detector, it is anticipated that this device would be well suited for sensitive detection of CO_2 , targeting the absorption at 2349 cm^{-1} . In a conventional CO_2 NDIR gas sensor the presence of CO_2 results in a drop in the transmitted power through the chamber at this 2349 cm^{-1} absorption. Although we are not measuring this drop in integrated power from the broadband detector directly, FTIR allows us to determine the change in absorption at 2349 cm^{-1} when CO_2 is introduced into the gas cell. Using the experimental setup outlined in the previous paragraph and detailed in the Methods section, we were able to validate this hypothesis as the NIREM device demonstrated similar sensitivity to CO_2 gas at both 50 and 400 ppm (Figure 5) as the blackbody source. It should be noted that even at the lowest concentration of the CO_2 calibration gas that was commercially available (50 ppm), we still detected over 1.5% absorption. This would imply that with this nonoptimized geometry that over an order of magnitude further reduction in CO_2 concentration should still be detectable in such a 15 cm cell as used here. From this comparison, it is clear that although the CO_2 absorption at 400 ppm is roughly equivalent for both sources, at 50 ppm it is slightly suppressed for the NIREM source, differing by just under 0.6% from the VACNT, however, such a difference is within the error of our measurements. Details regarding our error analysis can be found in the Supporting Information. Although these measurements were performed under a N_2 purge, there is still the possibility of background CO_2 fluctuations, which can cause

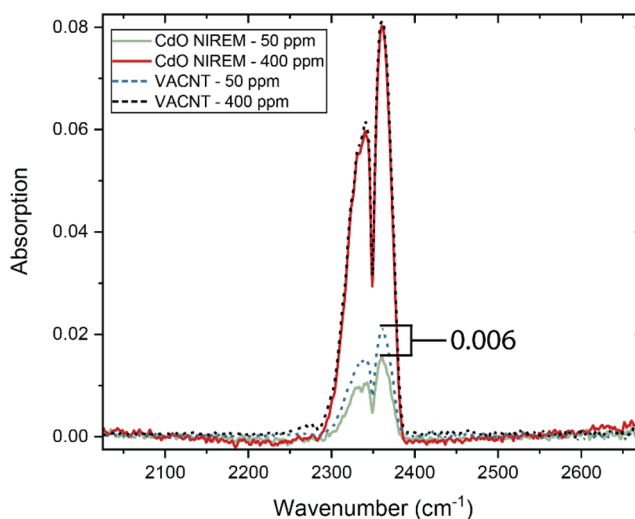


Figure 5. Absorption spectra at 250 °C comparing the performance of our CdO on PSS narrowband emitter to a blackbody at CO_2 concentrations of 400 and 50 ppm. Our narrowband emitter performs comparably to the blackbody sample even at low CO_2 concentrations (50 ppm).

slight deviations in the absorption magnitude. We would like to also note the aforementioned $\sim 200\text{ cm}^{-1}$ spectral detuning of the NIREM emission center frequency from the CO_2 absorption. Thus, with further optimization of the ENZ emission center frequency with respect to the CO_2 , a potential increase in sensitivity could be anticipated. Another point that should be raised is that the spectral line width of the NIREM emitter highlighted here is sufficiently broad that some spectral overlap would occur with other gases of interest featuring vibrational modes in the spectral vicinity of CO_2 , for instance N_2O . However, it is critical to point out that the device featured here by no means is representative of the narrowest CdO-based ENZ emitter/absorber line widths reported, as values as narrow as 307 cm^{-1} having been detailed previously.²⁷ For such narrower emission devices, this spectral overlap would be absent and thus the concept of filterless NDIR with our simple, low-cost NIREM emitter accessible. Furthermore, by implementing more advanced detection schemes, such as differential or modulated spectroscopies, or by further optimizing the ENZ resonance to the center frequency of the CO_2 absorption and increasing the PSS pitch to induce a narrowing of the emission line widths, increased selectivity, and potentially sensitivity, can be realized. We discuss potential routes toward achieving further reductions in the emission line width from our NIREM source in the Supporting Information.

CONCLUSION

Here, we have demonstrated the use of n-type In:CdO thin films grown on a PSS template offers several key advantages as mid-IR thermal emitter sources over thin flat CdO films discussed previously.²⁷ This results from the structured surface enabling near-unity emissivity of both *p*- and *s*-polarized light from the Berreman/ENZ-polariton modes, while redirecting the light from the Brewster angle ($\sim 65^\circ$) observed for flat films into a radiation pattern featuring >0.9 emissivity throughout the solid angle defined by $\pm 40^\circ$ off-normal. This NIREM device therefore offers a narrowband, near-perfect absorber with directional emission suitable for replacement of a

broadband blackbody source and bandpass filter pair typically employed within NDIR sensor platforms. The periodicity of the PSS template was observed to induce a strong diffractive mode that results in a large spectral narrowing at highly off-normal emission angles ($>40^\circ$), however, this was demonstrated to have minimal impact upon the emission peak at the Berreman condition at shallower angles and thus negligible impact upon the performance within an NDIR configuration. However, in advanced designs this diffractive coupling could be employed for reducing the radiated power at off-normal angles, further improving the spatial coherence and efficiency of the thermal emission. We, further, validate the performance of our NIREM device for such an NDIR application, observing similar sensitivity to trace level concentrations (50 ppm) of CO_2 gas as a blackbody currently employed in NDIR technologies. Our results, therefore, imply that such NIREM devices could provide a designer IR source for plug-and-play replacement of the blackbody/bandpass filter combo, thereby reducing NDIR device cost, complexity and potentially extending its functionality. The elimination of the bandpass filter offers the potential for realizing multiple NIREM devices within a single die, enabling serial detection of several molecules within the same gas cell, without requiring the inclusion of a bulky and expensive filter wheel or multiple NDIR devices. Furthermore, by using this approach, one could also envision advanced NDIR concepts whereby multiple vibrational resonances of more complicated analytes could be detected, thereby extending the NDIR concept from the current state of the art that is limited to simple molecules, such as CO_2 , CO , and CH_4 , to one compatible with more complicated gases, such as biological and chemical warfare agents, chemical byproducts, or environmental contaminants.

METHODS

Device Fabrication. In:CdO was deposited using reactive high power impulse magnetron sputtering (R-HiPIMS) from a metallic cadmium target. Doping was achieved through RF cosputtering from a metallic indium target. After deposition, samples were annealed at 700°C in an O_2 atmosphere. PSS substrates were sourced from Precision Micro-Optics, Inc.

Thermal Emission Measurements. Thermal emission was measured using a Bruker Vertex 70v FTIR, along with a custom external thermal emission setup. The sample was mounted on a vertically oriented hot plate equipped with a Venturi vacuum. Using a combination of micrometers and servo motors, this hot plate grants five degrees of freedom including xyz -position control, as well as polar and azimuthal angle control. An aperture was placed in the beam path between the hot plate and a focusing parabolic mirror with the purpose of limiting the detected solid angle to an approximate 0.5 cm diameter spot size, limiting emission that could be from the hot plate. A schematic showing the beam path for the angle-dependent thermal emission measurements can be found in Figure S7. The emission from the sample was then guided and collected through a KBr window and into the FTIR internal beam path. For polarized thermal emission measurements, a Ge polarizer was placed in the beam path between the mirror and pinhole (location noted in Figure S7) and measurements were conducted as is described for the unpolarized measurements. In this configuration the emitted signal passes through the interferometer block, taking the place of the spectrometer's internal broadband source which is turned off. The signal was measured using an IR laboratories

mercury–cadmium–telluride (MCT) detector. To calculate angle-dependent emissivity, thermal emission measurements were taken at every 10° from 0° to 80° for the CdO devices at 250°C . These measurements were then compared to the thermal emission measured from an emissivity standard at the same temperature and angle of emission. We used $500\ \mu\text{m}$ tall vertically aligned carbon nanotubes (VACNTs) grown on a Si substrate from an Fe-nanoparticle catalyst, grown by Nanotechlabs Inc., as an emissivity standard ($\epsilon \sim 0.97$). These VACNTs provide a high, consistent value for emissivity that is spectrally flat throughout the IR and stable with temperature. The signal collected by the MCT detector in these measurements contains the emission from both the sample, as well as the internal optics of the FTIR.

$$M(T_{\text{sample}}, T_{\text{ambient}}, \lambda, \theta) = R(T_{\text{ambient}}, \lambda)[S(T_{\text{sample}}, \lambda, \theta) + G(T_{\text{ambient}}, \lambda)] \quad (1)$$

Here M is the total measured signal, R is a response function for the internal and external optics, S is the signal originating from the sample and G is the “background” emission from the internal optics. Thus, in order to isolate the signal from the sample, a background measurement was taken by placing a gold mirror in the beam path in front of the hot plate. The resulting spectrum is a product of the response function R with the background emission G . Once the sample, emissivity standard and background emission have been measured we can rearrange eq 1.

$$R(T_{\text{ambient}}, \lambda)S_{\text{sample}}(T_{\text{sample}}, \lambda, \theta) = M_{\text{sample}}(T_{\text{sample}}, T_{\text{ambient}}, \lambda, \theta) - R(T_{\text{ambient}}, \lambda)G(T_{\text{ambient}}, \lambda) \quad (3)$$

$$R(T_{\text{ambient}}, \lambda)S_{\text{standard}}(T_{\text{sample}}, \lambda, \theta) = M_{\text{standard}}(T_{\text{sample}}, T_{\text{ambient}}, \lambda, \theta) - R(T_{\text{ambient}}, \lambda)G(T_{\text{ambient}}, \lambda) \quad (4)$$

The response function can be normalized out by taking the ratio of eq 3 to eq 4, and the emissivity relative to the standard can be determined.

$$\frac{R(T_{\text{ambient}}, \lambda)S_{\text{sample}}(T_{\text{sample}}, \lambda, \theta)}{R(T_{\text{ambient}}, \lambda)S_{\text{standard}}(T_{\text{sample}}, \lambda, \theta)} = \frac{S_{\text{sample}}(T_{\text{sample}}, \lambda, \theta)}{S_{\text{standard}}(T_{\text{sample}}, \lambda, \theta)} = \epsilon(T_{\text{sample}}, \lambda, \theta) \quad (5)$$

Note that this technique is much quicker than the conventional approach to measuring emissivity using FTIR and allows for multiple background measurements to be taken throughout the day. Therefore, fluctuations in the ambient temperature can be accounted for readily.

Simulations. Numerical simulations were performed using CST studio suite 2018. The carrier concentration and electron mobility of the CdO film were measured with Hall effect measurements in the Van der Pauw configuration. With these values, the dielectric function was calculated using the model presented in ref 26. A hexagonal unit cell was used for both the CdO on PSS and planar CdO devices and unit cell boundary

conditions were used. The geometry of the PSS cone was determined from SEM images taken at Vanderbilt University. The origin of the polar angle lies along the [1120] axis of the hexagonal unit cell. Simulated angle-dependent absorption spectra were obtained by taking the ratio of power loss in CdO to input waveguide port power. The Berreman/ENZ mode dispersion provided in Figure S4 was calculated using the Transfer Matrix Method.³⁸

Gas Cell Measurements. Transmission measurements of several concentrations of CO₂ were performed using a Bruker Vertex 70v FTIR along with a Pike short-path gas cell with KRS5 windows. Just as with the angle dependent thermal emission measurements, the CdO PSS NIREM or the VACNT blackbody standard was used in lieu of the global source in the FTIR. The beam path for these measurements is shown in Figure S7. Here, our sample is placed on a temperature controller located at a backport of the FTIR. The sample was heated to 250 °C and the emission was directed into the FTIR at an angle normal from the sample surface. The gas cell was placed in the sample compartment of the FTIR which was under a constant N₂ purge. The remainder of the FTIR bench was also under a constant N₂ purge. The gas cell is equipped with 4 ports, 2 external ports for N₂ purging of the areas outside of the gas cell windows and 2 internal (inlet and outlet) ports for supplying gas to the gas cell. The gas cell was initially purged with N₂ until the spectrum from the sample reached a steady state. The gas cell was then sealed (outlet valve shut) and a background transmission measurement was recorded under N₂ purge. We, then, opened the outlet valve and used CO₂/N₂ mixture calibration gases with varying CO₂ concentrations from GASCO to fill the gas cell. As with the background spectrum, we allowed the CO₂/N₂ calibration gas to flow until the spectrum reached a steady state and then closed the outlet valve and proceeded to collect our measurement.

■ ASSOCIATED CONTENT

■ Supporting Information

The Supporting Information is available free of charge at <https://pubs.acs.org/doi/10.1021/acsp Photonics.0c01432>.

Polarized thermal emission measurement; simulation results and discussion of the PSS pitch dependence; calculated dispersion relation for Berreman/ENZ supporting CdO film; discussion of the spectral bandwidth of the CdO NIREM; SEM images of the CdO planar film and NIREM; beam diagrams of measurements; and error analysis for CO₂ sensing measurements (PDF)

■ AUTHOR INFORMATION

Corresponding Author

Joshua D. Caldwell – Department of Mechanical Engineering, Vanderbilt University, Nashville, Tennessee 37212, United States; orcid.org/0000-0003-0374-2168; Email: josh.caldwell@vanderbilt.edu

Authors

Alyssa Livingood – Department of Electrical and Computer Engineering, University of Kentucky, Lexington, Kentucky 40506, United States; Research Experience for Undergraduates (REU) program, Vanderbilt Institute for

Nanoscale Science and Engineering (VINSE), Nashville, Tennessee 37212, United States

J. Ryan Nolen – Interdisciplinary Materials Science Program, Vanderbilt University, Nashville, Tennessee 37212, United States; orcid.org/0000-0002-8774-7734

Thomas G. Folland – Department of Mechanical Engineering, Vanderbilt University, Nashville, Tennessee 37212, United States; Department of Physics and Astronomy, The University of Iowa, Iowa City, Iowa 52242, United States; orcid.org/0000-0002-4665-235X

Lauren Potechin – Department of Mechanical Engineering, Vanderbilt University, Nashville, Tennessee 37212, United States

Guanyu Lu – Department of Mechanical Engineering, Vanderbilt University, Nashville, Tennessee 37212, United States; orcid.org/0000-0001-8960-0464

Scott Criswell – Department of Electrical Engineering, Vanderbilt University, Nashville, Tennessee 37212, United States

Jon-Paul Maria – The Pennsylvania State University, State College, Pennsylvania 16801, United States

Christopher T. Shelton – Third Floor Materials, Raleigh, North Carolina 27695, United States

Edward Sachet – Third Floor Materials, Raleigh, North Carolina 27695, United States

Complete contact information is available at:

<https://pubs.acs.org/10.1021/acsp Photonics.0c01432>

■ Author Contributions

■ A.L. and J.R.N. contributed equally.

■ Notes

The authors declare no competing financial interest.

■ ACKNOWLEDGMENTS

Support for J.D.C. and J.R.N. were provided by the Office of Naval Research under grant number N00014-18-1-2107. A.L. was supported through a Research Experience for Undergraduates (REU) program funded by the National Science Foundation under grant number 1560414 that was administered by the Vanderbilt Institute for Nanoscience and Engineering (VINSE). T.G.F. acknowledges support from Third Floor Materials, Inc. S.C. was supported jointly through the Science Mathematics and Research for Transformation (SMART) Scholarship sponsored by Naval Surface Warfare Center Crane and the Crane PhD Fellowship sponsored by Naval Surface Warfare Center Crane. J.-P.M. acknowledges support from Army Research Office Grant W911NF-16-1-0406.

■ REFERENCES

- (1) Sberveglieri, G., Ed. *Gas Sensors: Principles, Operation and Developments*; Kluwer: Boston, 1992.
- (2) Meyer, J. R.; Vurgaftman, I.; Canedy, C. L.; Bewley, W. W.; Kim, C. S.; Merritt, C. D.; Warren, M. V.; Kim, M. In-Plane Resonant-Cavity Infrared Photodetectors with Fully-Depleted Absorbers. *US10062794B2*, 2019.
- (3) Tan, X.; Zhang, H.; Li, J.; Wan, H.; Guo, Q.; Zhu, H.; Liu, H.; Yi, F. Non-Dispersive Infrared Multi-Gas Sensing via Nanoantenna Integrated Narrowband Detectors. *Nat. Commun.* **2020**, *11* (1), 1–9.
- (4) Hodgkinson, J.; Tatam, R. P. Optical Gas Sensing: A Review. *Meas. Sci. Technol.* **2013**, *24*, 012004.
- (5) Lochbaum, A.; Dorodnyy, A.; Koch, U.; Koepfli, S. M.; Volk, S.; Fedoryshyn, Y.; Wood, V.; Leuthold, J. Compact Mid-Infrared Gas

Sensing Enabled by an All-Metamaterial Design. *Nano Lett.* **2020**, *20* (6), 4169–4176.

(6) Koppens, F. H. L.; Mueller, T.; Avouris, P.; Ferrari, A. C.; Vitiello, M. S.; Polini, M. Photodetectors Based on Graphene, Other Two-Dimensional Materials and Hybrid Systems. *Nat. Nanotechnol.* **2014**, *9* (10), 780–793.

(7) Folland, T. G.; Nordin, L.; Wasserman, D.; Caldwell, J. D. Probing Polaritons in the Mid- to Far-Infrared. *J. Appl. Phys.* **2019**, *125* (19), 191102.

(8) De Zoysa, M.; Asano, T.; Mochizuki, K.; Oskooi, A.; Inoue, T.; Noda, S. Conversion of Broadband to Narrowband Thermal Emission through Energy Recycling. *Nat. Photonics* **2012**, *6* (8), 535–539.

(9) Laroche, M.; Carminati, R.; Greffet, J. Coherent Thermal Antenna Using a Photonic Crystal Slab Coherent Thermal Antenna Using a Photonic Crystal Slab. *Phys. Rev. Lett.* **2014**, DOI: 10.1103/PhysRevLett.96.123903.

(10) Inoue, T.; De Zoysa, M.; Asano, T.; Noda, S. High-Q Mid-Infrared Thermal Emitters Operating with High Power-Utilization Efficiency. *Opt. Express* **2016**, *24*, 15101.

(11) Greffet, J. J.; Carminati, R.; Joulain, K.; Mulet, J. P.; Mainguy, S.; Chen, Y. Coherent Emission of Light by Thermal Sources. *Nature* **2002**, *416* (6876), 61–64.

(12) Lu, G.; Nolen, R. J.; Folland, T. G.; Tadjer, M.; Walker, D. G.; Caldwell, J. D. Narrowband Polaritonic Thermal Emitters Driven by Waste-Heat. *ACS Omega* **2020**, *5*, 10900.

(13) Wang, T.; Li, P.; Chigrin, D. N.; Giles, A. J.; Bezares, F. J.; Glembocki, O. J.; Caldwell, J. D.; Taubner, T. Phonon-Polaritonic Bowtie Nanoantennas: Controlling Infrared Thermal Radiation at the Nanoscale. *ACS Photonics* **2017**, *4*, 1753–1760.

(14) Schuller, J. A.; Taubner, T.; Brongersma, M. L. Optical Antenna Thermal Emitters. *Nat. Photonics* **2009**, *3*, 658–661.

(15) Howes, A.; Nolen, J. R.; Caldwell, J. D.; Valentine, J. Near-Unity and Narrowband Thermal Emissivity in Balanced Dielectric Metasurfaces. *Adv. Opt. Mater.* **2020**, *8* (4), 1901470.

(16) Mason, J. A.; Smith, S.; Wasserman, D. Strong Absorption and Selective Thermal Emission from a Midinfrared Metamaterial. *Appl. Phys. Lett.* **2011**, *98*, 241105.

(17) Baranov, D. G.; Xiao, Y.; Nechepurenko, I. A.; Krasnok, A.; Alù, A.; Kats, M. A. Nanophotonic Engineering of Far-Field Thermal Emitters. *Nat. Mater.* **2019**, *18* (9), 920–930.

(18) Caldwell, J. D.; Glembocki, O. J.; Francescato, Y.; Sharac, N.; Giannini, V.; Bezares, F. J.; Long, J. P.; Owrutsky, J. C.; Vurgaftman, I.; Tischler, J. G.; Wheeler, V. D.; Bassim, N. D.; Shirey, L. M.; Kasica, R.; Maier, S. A. Low-Loss, Extreme Subdiffraction Photon Confinement via Silicon Carbide Localized Surface Phonon Polariton Resonators. *Nano Lett.* **2013**, *13* (8), 3690–3697.

(19) Liu, X.; Tyler, T.; Starr, T.; Starr, A. F.; Jokerst, N. M.; Padilla, W. J. Taming the Blackbody with Infrared Metamaterials as Selective Thermal Emitters. *Phys. Rev. Lett.* **2011**, *107* (4), 4–7.

(20) Landy, N. I.; Sajuyigbe, S.; Mock, J. J.; Smith, D. R.; Padilla, W. J. *Phys. Rev. Lett.* **2008**, DOI: 10.1103/PhysRevLett.100.207402.

(21) Lochbaum, A.; Fedoryshyn, Y.; Dorodnyy, A.; Koch, U.; Hafner, C.; Leuthold, J. On-Chip Narrowband Thermal Emitter for Mid-IR Optical Gas Sensing. *ACS Photonics* **2017**, *4* (6), 1371–1380.

(22) Vassant, S.; Hugonin, J.-P.; Marquier, F.; Greffet, J.-J. Berreman Mode and Epsilon near Zero Mode. *Opt. Express* **2012**, *20* (21), 23971–23977.

(23) Campione, S.; Brener, I.; Marquier, F. Theory of Epsilon-near-Zero Modes in Ultrathin Films. *Phys. Rev. B: Condens. Matter Mater. Phys.* **2015**, *91*, 121408.

(24) Kelley, K. P.; Sachet, E.; Shelton, C. T.; Maria, J. P. High Mobility Yttrium Doped Cadmium Oxide Thin Films. *APL Mater.* **2017**, *5* (7), 076105.

(25) Runnerstrom, E. L.; Kelley, K. P.; Sachet, E.; Shelton, C. T.; Maria, J. P. Epsilon-near-Zero Modes and Surface Plasmon Resonance in Fluorine-Doped Cadmium Oxide Thin Films. *ACS Photonics* **2017**, *4*, 1885.

(26) Nolen, J. R.; Runnerstrom, E. L.; Kelley, K. P.; Luk, T. S.; Folland, T. G.; Cleri, A.; Maria, J.-P.; Caldwell, J. D. Ultraviolet to

Far-Infrared Dielectric Function of n-Doped Cadmium Oxide Thin Films. *Phys. Rev. Mater.* **2020**, *4* (2), 1–10.

(27) Kelley, K. P.; Runnerstrom, E. L.; Sachet, E.; Shelton, C. T.; Grimley, E. D.; Klump, A.; Lebeau, J. M.; Sitar, Z.; Suen, J. Y.; Padilla, W. J.; Maria, J.-P. Multiple Epsilon-Near-Zero Resonances in Multilayered Cadmium Oxide: Designing Metamaterial-Like Optical Properties in Monolithic Materials. *ACS Photonics* **2019**, *6* (5), 1139–1145.

(28) Sachet, E.; Shelton, C. T.; Harris, J. S.; Gaddy, B. E.; Irving, D. L.; Curtarolo, S.; Donovan, B. F.; Hopkins, P. E.; Sharma, P. A.; Sharma, A. L.; Ihlefeld, J.; Franzen, S.; Maria, J. P. Dysprosium-Doped Cadmium Oxide as a Gateway Material for Mid-Infrared Plasmonics. *Nat. Mater.* **2015**, *14* (4), 414–420.

(29) Chao, S. H.; Yeh, L. H.; Wu, R. T.; Kawagishi, K.; Hsu, S. C. Novel Patterned Sapphire Substrates for Enhancing the Efficiency of GaN-Based Light-Emitting Diodes. *RSC Adv.* **2020**, *10* (28), 16284–16290.

(30) Malerba, M.; Alabastri, A.; Miele, E.; Zilio, P.; Patrini, M.; Bajoni, D.; Messina, G. C.; Dipalo, M.; Toma, A.; Proietti Zaccaria, R.; De Angelis, F. 3D Vertical Nanostructures for Enhanced Infrared Plasmonics. *Sci. Rep.* **2015**, *5*, 16436.

(31) Nikitin, A. G.; Kabashin, A. V.; Dallaporta, H. Plasmonic Resonances in Diffractive Arrays of Gold Nanoantennas: Near and Far Field Effects. *Opt. Express* **2012**, *20* (25), 27941.

(32) Kravets, V. G.; Schedin, F.; Grigorenko, A. N. Extremely Narrow Plasmon Resonances Based on Diffraction Coupling of Localized Plasmons in Arrays of Metallic Nanoparticles. *Phys. Rev. Lett.* **2008**, *101*, 087403.

(33) Giannini, V.; Francescato, Y.; Amrania, H.; Phillips, C. C.; Maier, S. A. Fano Resonances in Nanoscale Plasmonic Systems: A Parameter-Free Modeling Approach. *Nano Lett.* **2011**, *11* (7), 2835–2840.

(34) Simpkins, B. S.; Long, J. P.; Glembocki, O. J.; Guo, J.; Caldwell, J. D.; et al. Pitch-Dependent Resonances and near-Field Coupling in Infrared Nanoantenna Arrays. *Opt. Express* **2012**, *20*, 27725.

(35) Adato, R.; Yanik, A. A.; Amsden, J. J.; Kaplan, D. L.; Omenetto, F. G.; Hong, M. K.; Erramilli, S.; Altug, H. Ultra-Sensitive Vibrational Spectroscopy of Protein Monolayers with Plasmonic Nanoantenna Arrays. *Proc. Natl. Acad. Sci. U. S. A.* **2009**, *106* (46), 19227–19232.

(36) Adato, R.; Artar, A.; Erramilli, S.; Altug, H. *Nano Lett.* **2013**, *13*, 2584.

(37) Linstrom, P. J., Mallard, W. G., Eds. NIST Standard Reference Database Number 69. *NIST Chemistry WebBook*; National Institute of Standards and Technology: Gaithersburg, MD, 2018.

(38) Passler, N. C.; Paarmann, A. Generalized 4×4 Matrix Formalism for Light Propagation in Anisotropic Stratified Media: Study of Surface Phonon Polaritons in Polar Dielectric Heterostructures. *J. Opt. Soc. Am. B* **2017**, *34* (10), 2128–2139.